Chapter 5

Digital elevation model generation from satellite interferometric synthetic aperture radar

Zhong Lu, Hyung-Sup Jung, Lei Zhang, Wonjin Lee, Chang-Wook Lee, and Daniel Dzurisin

CONTENTS

An accurate digital elevation model (DEM) is a critical data set for characterizing the natural landscape, monitoring natural hazards, and georeferencing satellite imagery. The ideal interferometric synthetic aperture radar (InSAR) configuration for DEM production is a single-pass two-antenna system. Repeat-pass single-antenna satellite InSAR imagery, however, also can be used to produce useful DEMs. DEM generation from InSAR is advantageous in remote areas where the photogrammetric approach to DEM generation is hindered by inclement weather conditions. There are many sources of errors in DEM generation from repeat-pass InSAR imagery, for example, inaccurate determination of the InSAR baseline, atmospheric delay anomalies, and possible surface deformation because of tectonic, volcanic, or other sources during the time interval spanned by the images. This chapter presents practical solutions to identify and remove various artifacts in repeat-pass satellite InSAR images to generate a high-quality DEM.

5.1 INTRODUCTION

An accurate digital elevation model (DEM) is a critical data set for the studies of hydrology, glaciology, forestry, geology, oceanography, and land environment, and it has been used extensively as a base layer in hazards-related geographic information systems (GIS) to model natural hazards (Maune, 2001). In volcano monitoring, DEMs calculated before, during, and after an eruption can be used to understand the eruption progress, estimate the thickness and volume of lava flows or ash deposits, and simulate potential mudflows. In glacier monitoring, DEMs can be used to determine the magnitude and direction of the gravitational force that drives ice flow and ice dynamics. Timely DEMs can be important for characterizing hazards associated with earthquakes, landslides, flooding, snow avalanches, and other processes. In addition, DEMs are indispensible in geocoding satellite images during geometric processing so that the georeferenced satellite images can be used as GIS data sets for hazard monitoring and resource management.

Interferometric synthetic aperture radar (InSAR) utilizes two or more SAR images of the same area to extract the landscape topography and patterns of surface change (Massonnet and Feigl, 1998; Rosen et al., 2000; Lu et al. 2007). An InSAR image, or interferogram, can be produced by combining the phase components of two coregistered SAR images of the same area acquired from similar vantage points. An interferogram formed in this way depicts range changes between the radar and the ground resolution elements, and can be used to derive both the landscape topography and subtle changes in surface elevation if the SAR images are acquired at different times.

For InSAR purposes, the spatial separation between two SAR antennas, or between two vantage points of the same SAR antenna, is called the baseline. Two antennas can be mounted on a single platform for simultaneous, single-pass InSAR. This is the usual implementation for airborne and shuttle systems, such as topographic SAR (TOPSAR) (Zebker et al., 1992) and shuttle radar topography mission (SRTM) (Farr et al., 2007). Single-pass two-antenna InSAR is the ideal configuration for generating high-resolution, precise DEMs over large regions. For satellite systems, however, SAR images used for InSAR mapping can be acquired only by using a single antenna in nearly identical repeating orbits. In this case, known as repeat-pass InSAR, even though successive observations of the target area are separated in time, the SAR observations will be highly correlated if the backscattering properties of the surface have not changed in the interim. This is the typical implementation for past and present satellite SAR sensors, including European Space Agency (ESA) European Remote-sensing Satellite 1 (ERS-1) (operated 1991–2000, C-band, wavelength $\lambda = 5.66$ centimeter [cm]), Japan Aerospace Exploration Agency (JAXA) Japanese

Earth Resources Satellite 1 (JERS-1) (1992–1998, *L*-band, λ = 23.5 cm), ESA European Remote-sensing Satellite 2 (ERS-2) (1995–2011, *C*-band, λ = 5.66 cm), Canadian Space Agency (CSA) Canadian Radar Satellite 1 (RADARSAT-1) (1995–present, *C*-band, λ = 5.66 cm), ESA European Environmental Satellite (Envisat) (2002–present, *C*-band, λ = 5.63 cm), JAXA Japanese Advanced Land Observing Satellite (ALOS) (2006–2011, *L*-band, λ = 23.6 cm), CSA RADARSAT-2 (2007–present, *C*-band, λ = 5.55 cm), German Aerospace Agency (DLR) TerraSAR-X (2007–present, *X*-band, λ = 3.1 cm), Italian COSMO-SkyMed satellite constellation (2007–present, *X*-band, λ = 3.1 cm), and DLR TerraSAR-X Add-on for Digital Elevation Measurements (TanDEM-X) (2010–present, *X*-band, λ = 3.1 cm).

Repeat-pass InSAR has proven capable of mapping ground-surface deformation with subcentimeter accuracy for *X*-band and *C*-band sensors (λ =2–8 cm), or few-centimeter accuracy for *L*-band sensors (λ = 15–30 cm) at spatial resolutions of tens-of-meters over image swaths tens to hundreds of kilometers wide (Massonnet and Feigl, 1998; Lu, 2007). Because spatial baselines of repeat-pass satellite radars are not zero, however, the derived interferograms contain information about the landscape topography. Therefore, repeat-pass InSAR can be used to generate DEMs as well (e.g., Small et al., 1995; Zebker et al., 1995; Ruffino et al., 1998; Sansosti et al., 1999; Hensley et al., 2001; Lu et al., 2003).

This chapter discusses techniques and issues related to DEM generation from repeat-pass satellite InSAR images. The chapter also addresses the two main reasons to use this method. First, past, current, and near-future radar satellites all are equipped with a single antenna, providing a large volume of archived imagery that can be exploited to generate DEMs. Second, InSAR is probably the most practical means of constructing DEMs of areas where the photogrammetric approach to DEM generation is hindered by inclement weather or difficult logistical factors (Maune, 2001).

5.2 DEM GENERATION FROM REPEAT-PASS INSAR

5.2.1 Technical issues on DEM generation from repeat-pass InSAR

InSAR processing involves the combination of two or more complex SAR images of the same terrain, and typically includes steps such as precise registration of an interferometric SAR image pair, interferogram generation, removal of curved Earth phase trend, adaptive filtering, phase unwrapping, precision estimate of interferometric baseline, and generation of a surface deformation image or DEM map (e.g., Lu, 2007).

Generally speaking, the phase of an interferogram from two repeat-pass SAR images is a superposition of phases resulting from several processes:

$$\Delta\phi(x) = -\frac{4\pi}{\lambda}\left[\Delta d(x) + \frac{B_{\perp}}{R\sin\theta}h(x)\right] + \Delta\phi_{\text{atmo}}(x) + \Delta\phi_{\text{orbit}}(x) + \Delta\phi_{\text{n}}(x), \quad (5.1)$$

where $\Delta\phi$ is the InSAR phase measurement, x is the pixel location index, λ the radar wavelength, R is the slant range distance, $B_{\perp}$ the perpendicular baseline, θ the SAR look angle, Δd the surface displacement in the radar look direction, h the topographic height, $\Delta\phi_{\text{atmo}}$ the atmospheric phase delay artifact, $\Delta\phi_{\text{orbit}}$ the baseline error, and $\Delta\phi_{\text{n}}$ the phase noise resulting from temporal decorrelation and other noise sources. Because our goal is to derive an accurate DEM (h) based on the observed InSAR phase ($\Delta\phi$), the other phase components (Δd, $\Delta\phi_{\text{atmo}}$, $\Delta\phi_{\text{orbit}}$, and $\Delta\phi_{\text{n}}$) are treated as error sources.

Before we discuss the error sources that affect DEM accuracy, let us briefly look at the sensitivity of the InSAR phase measurement ($\Delta\phi$) to the surface deformation (Δd) and topographic height (h). If we assume that the error terms related to atmosphere, orbit, and noise are zero, the interferogram phase (after removing the contribution from the effect of ellipsoid Earth (Lu, 2007) can be simplified as follows:

$$\Delta\phi \approx -\frac{4\pi}{\lambda}\Delta d - \frac{4\pi}{\lambda}\frac{B_{\perp}}{H\tan\theta}h, \quad (5.2)$$

where H is the satellite altitude above a reference Earth surface. If Δd is negligible in Equation 5.2, the interferogram phase value in Equation 5.2 can be used to calculate height h. This is the principle of how InSAR phase measurements can be used to produce a DEM. For the ESA ERS-1/-2 satellites, H is about 800 kilometers (km), θ is about 23 degrees, λ is 5.66 cm, and $B_{\perp}$ should be less than the critical baseline, beyond which an interferogram loses coherence (Massonnet and Feigl, 1998). Therefore, Equation 5.2 can be approximated as follows:

$$\Delta\phi \approx -\frac{4\pi}{\lambda}\Delta d - \frac{2\pi}{9{,}600}B_{\perp}h. \quad (5.3)$$

For an interferogram with $B_{\perp}$ of 100 meters (m), which is within the critical baseline of 1,100 m for ERS-1/-2 SAR, 1 m of topographic relief produces a phase value of about 4 degrees. Producing the same phase value, however, requires only 0.3 millimeters (mm) of surface deformation. Therefore, it is evident that the interferogram phase value can be much more sensitive to changes in topography (i.e., the surface deformation Δd) than to the

topography itself (i.e., *h*). That explains why repeat-pass InSAR is capable of detecting surface deformation at theoretical subcentimeter accuracy (Lu, 2007). The accuracy of a DEM derived from repeat-pass InSAR, however, can only reach to meter level if artifacts in InSAR images are negligible. Several specific error sources can affect DEM accuracy.

First, a major error source in repeat-pass InSAR DEM generation is the baseline uncertainty due to inaccurate determination of SAR antenna positions. Errors in this value propagate into very large systematic errors of terrain height. If precision satellite orbit data are available, they should be used for InSAR processing. The interferogram baseline should always be refined using control points or areas with known elevations (or from an existing low-resolution DEM) via a least squares approach (Rosen et al., 1996). In this approach, areas (or pixels) of the interferogram that are used to refine the baseline should have negligible deformation, or known deformation, obtained from an independent source.

Second, because the phase of the radar signal is used to calculate elevation, errors in phase measurement can contribute to the topographic inaccuracy. Random phase errors generally are caused by thermal noise in the SAR system and by decorrelation or incoherence that is in turn caused by volume scattering and environmental change of the imaged surface. Surface changes tend to accumulate with time, so a longer time interval between passes of an InSAR pair can result in poorer coherence (Lu and Freymueller, 1998). The elevation error from a given phase error is inversely proportional to the perpendicular component of baseline length (see Equation 5.2). The topography effect does not appear if the baseline is zero and the sensitivity of interferometric phase value to the topography increases with lengthening baseline. Therefore longer baselines are necessary for accurate DEMs. Unless the volume scattering is negligible and an ideal spectrum filtering is applied (Gatelli et al., 1994), longer baselines can cause geometric decorrelation. This results in an increase in the phase error and consequently the elevation error. Therefore, for DEM generation, we should choose interferograms with the largest available baseline within the limit of correlation.

A third critical error source in deriving DEMs from repeat-pass InSAR is atmospheric delay anomalies caused by small variations in the index of refraction along the line of propagation (Goldstein, 1997; Gray et al., 2000). Changes in the total electron content of the ionosphere as well as changes in water vapor content of the troposphere will compromise the quality of the observed interferogram by varying the phase signals. Height errors due to atmospheric anomalies are typically not as large as those resulting from baseline errors, but they are less systematic and harder to detect. Ionosphere artifacts are more severe on longer wavelength (e.g., *L*-band) and methods of reducing ionospheric artifacts are still an active research topic. The methods to mitigate effects of atmospheric delays in InSAR data can be grouped as follows: (a) integration of InSAR observations with data

from dense GPS networks (e.g., Emardson et al., 2003); (b) integration with multispectrum atmospheric water vapor observations (e.g., precipitable water vapor products from moderate resolution imaging spectroradiometer [MODIS] or medium resolution imaging spectrometer [MERIS]; Li et al., 2003); (c) time-series InSAR techniques (e.g., Ferretti et al., 2001; Berardino et al., 2002); (d) integration with short-term predictions from operational weather models (e.g., Foster et al., 2006; Gong et al., 2011); and (e) some combination of methods a through d. In remote and cloud-prone areas, complex environmental conditions typically limit the feasibility of methods a and b. Method c exploits the statistical properties of atmospheric phase components in time-series SAR observations. Its limitation is that it requires a large number of SAR acquisitions and prior knowledge of radar backscattering properties of the study area to properly set parameters during data processing. Method d, utilizing numerical weather models, is not limited by the aforementioned facts, but it requires sufficient initial boundary data and is also computation intensive (Gong et al., 2011). To minimize atmospheric artifacts in repeat-pass InSAR DEM generation, the most practical approach is to choose interferograms with relatively long baselines, as the effect of atmospheric anomalies on DEM heights is inversely proportional to baseline length, and to average multiple interferograms to reduce the atmospheric effects.

Finally, we must take into account any possible surface deformation resulting from tectonic, volcanic, or other loading sources over the time interval spanned by repeat-pass interferograms (Lu et al., 2003). Even for areas without tectonic motions, ground surface deformation resulting from variations of groundwater tables (e.g., Lu and Danskin, 2001), permafrost (Rykhus and Lu, 2008), and changes in soil moisture (Gabriel et al., 1989) should be considered. Interferograms with shorter temporal separations are preferred for generating DEMs. The ESA ERS-1/ERS-2 Tandem data meet this requirement in most cases. During the ERS-1/ERS-2 Tandem mission in 1995–1996, interferometric pairs were acquired by ERS-1 and ERS-2 satellites, each of which repeat every 35 days, to follow one another by 1 day in the same orbital geometry. Thus, a point on the surface was imaged by one satellite (ERS-1) on a given day and by the other satellite (ERS-2) on the following day. In cases in which tandem data are not available or not appropriate for DEM generation, deformation rates should be estimated independently and removed from the interferograms used for DEM production.

5.2.2 DEM generation from repeat-pass InSAR: A case study

In this case study, we demonstrate how repeat-pass InSAR images were used to derive DEMs of Okmok volcano, Umnak Island, Alaska, and how

InSAR-derived DEMs of Okmok both before and after its 1997 eruption were used to estimate lava flow thickness.

Okmok volcano, a broad shield topped with a 10 km wide caldera, occupies most of the northeastern end of Umnak Island, Alaska (see Figure 5.1). The caldera was formed by eruptions about between 8,000 and 2,000 years ago (Miller et al., 1988). A dozen eruptions have occurred in the 20th century, including one in 1997. All of these eruptions originated from Cone A, a cinder cone located on the southern edge of the caldera floor. Abundant ash emissions and mafic lava flows originating from Cone A have spread across the caldera floor. The 1997 eruption of Okmok volcano began in early February and ended in late April. The eruption was a moderate Hawaiian to Strombolian type with an ash plume reaching to 10,000 m above sea level, and erupted basaltic a'a' lava flows traveled a few kilometers from cone A. ERS-1/-2 InSAR data were used to map the preeruptive, coeruptive, and posteruptive deformation (Lu et al., 1998, 2000, 2005, 2010a). The authors measured about 140 cm of subsidence associated with the 1997 eruption of Okmok volcano. This subsidence occurred during an interval beginning 16 months before the eruption and ending 5 months after the

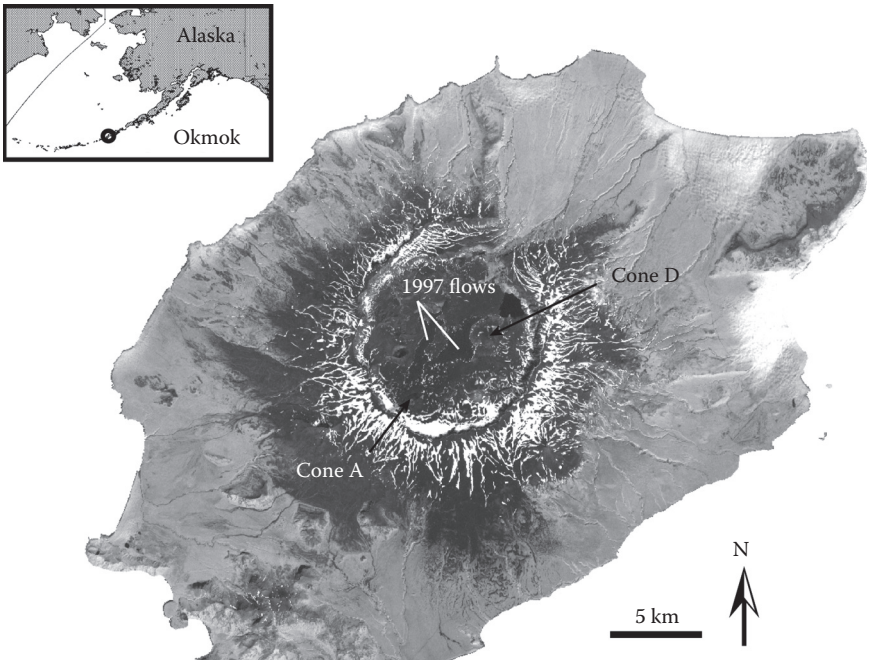

Figure 5.1 **(See color insert.)** A terrain-corrected, georeferenced Landsat-7 Enhanced Thematic Mapper+ image (Band 8) of Okmok volcano, Umnak Island, Alaska. The image was acquired on August 18, 2000. The location of Okmok volcano relative to the rest of Alaska and the Aleutian arc is shown in the inset.

eruption. This subsidence was preceded by about 18 cm of uplift between 1992 and 1995, centered in the same location as the coeruptive subsidence source, and was followed by progressive inflation afterward (Lu et al., 2010a).

Because SRTM was acquired in February 2000 (Farr et al., 2007), we can use the SRTM DEM (see Figure 5.2) to represent Okmok's topography after the 1997 eruption. Here, utilizing multitemporal repeat-pass InSAR images from ERS-1/ERS-2, we constructed a DEM that represents the topography of Okmok volcano before the 1997 eruption. The difference of the preeruption and posteruption DEMs can render a three-dimensional (3D) distribution of the lava flows erupted in 1997.

As discussed, to produce accurate DEMs using repeat-pass ERS-1 and ERS-2 SAR images, atmospheric anomalies need to be carefully considered, because images used for InSAR processing are acquired at different times. Also, a compromise between baseline and interferometric coherence has to be made to select InSAR pairs suitable for DEM generation. Finally, for tectonically or volcanically active regions, any deformation signal must be removed from the interferograms used for DEM generation.

On the basis of the available ERS-1/-2 SAR images acquired before the 1997 eruption at Okmok volcano, we generated seven interferograms. Three interferograms were used to estimate ground surface deformation

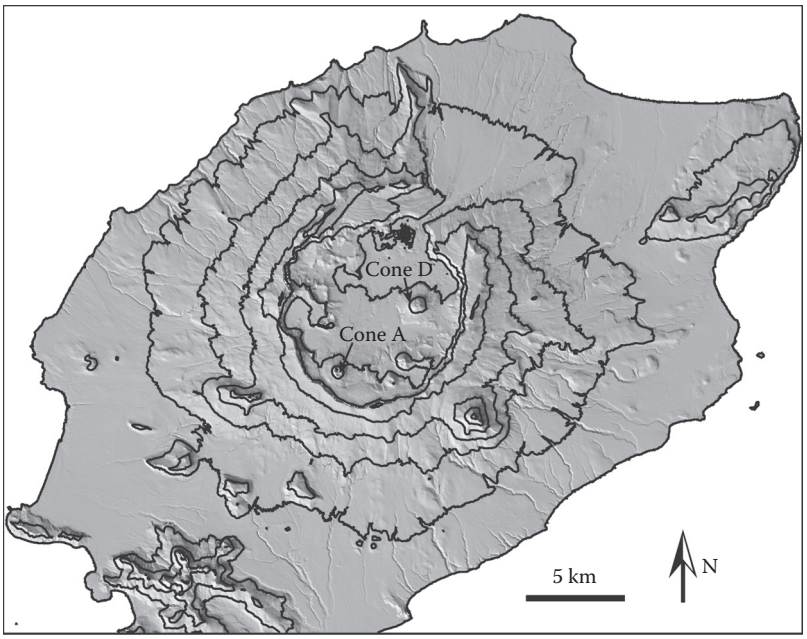

Figure 5.2 Shaded relief image created from the 1-arc-second SRTM DEM of Okmok volcano, Alaska. The contour interval is 200 m.

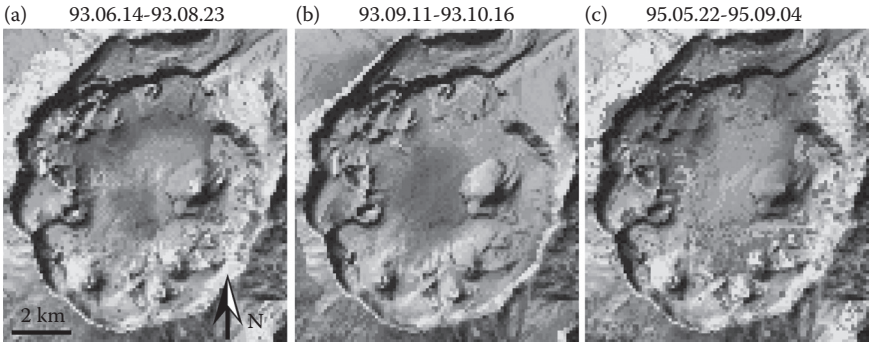

Figure 5.3 **(See color insert.)** Deformation interferograms of Okmok volcano during three different time periods: (a) June 14 to August 23, 1993, with the perpendicular component of baseline, $B_\perp$, equal to 32 m; (b) September 11 to October 16, 1993, with $B_\perp = 25$ m; (c) May 22, and September 4, 1995, with $B_\perp = 22$ m. The inflation was estimated and removed from those interferograms used for DEM generation (see Table 5.1). A full cycle of colors represents 28 mm surface deformation along the satellite look direction. Areas of coherence loss are uncolored.

(see Figure 5.3) and the other four InSAR images (see Table 5.1) were used for DEM generation. In general, interferometric coherence is maintained reasonably well within the caldera and it is lost around the caldera rim where terrain is rugged and persistent snow patches are present. This is sufficient as we only needed to determine a preeruption DEM within the caldera floor, part of which is covered by lava flows from the 1997 eruption. The caldera floor subsided about 1.4 m during the April 1997 eruption, and inflated at about 10 cm/year from 1997 to 2000 (Lu et al., 1998, 2000, 2005, 2010a). Therefore, over areas that are not covered by 1997 lava flows, the topographic change between 1993 (or 1995) (i.e., preeruption DEM) and 2000 (i.e., posteruption DEM) is about 1.1 m at maximum.

We produced three InSAR images with small baselines (see Figure 5.3), which were used to estimate and remove the volcanic inflation during the time periods of the interferograms used for DEM generation (see Table 5.1). Because these interferograms (see Figure 5.3) have very small baselines, they are insensitive to DEM errors. Therefore, we can use either the posteruption

Table 5.1 Interferometric data acquisition parameters for DEM generation over okmok volcano

Orbit 1	*Orbit 2*	*Date 1*	*Date 2*	$B_\perp$ *(m)*
ERS1_22376	ERS2_02703	October 25, 1995	October 26, 1995	83
ERS1_10781	ERS1_11282	August 7, 1993	September 11, 1993	403
ERS1_11783	ERS1_12284	October 16, 1993	November 20, 1993	395
ERS1_11010	ERS1_11511	August 23, 1993	September 27, 1993	690

SRTM DEM (see Figure 5.2) or the preexisting low-resolution DEM (Lu et al., 1998) to remove topographic effects for deformation analysis. Because these interferograms have shorter time separation and are temporally close to the interferograms used for preeruption DEM generation, they better portray the deformation that occurred in the interferograms used for DEM generation (see Table 5.1).

To remove the deformation signal from the DEM interferograms (see Table 5.1), we estimated the location and magnitude of the inflation source responsible for the surface deformation using a point source model embedded in an elastic homogeneous half-space (Mogi, 1958). We interpreted this source to represent a magma chamber at depth. Deformation predicted by the best-fitting model was then removed from the DEM interferograms. We concluded that the magma body was located over the center of the caldera at about 3 km deep and that the maximum inflation was about 18 mm and 4 mm per 35 days during the summers of 1993 and 1995, respectively.

Errors in deformation estimates will transfer into errors in the created DEM. If we neglect atmosphere, baseline, and noise terms in Equation 5.1, we can obtain the following:

$$\Delta h = -\frac{\lambda}{4\pi}\frac{H \tan\theta}{B_{\perp}}\Delta\phi, \tag{5.4}$$

where Δh is the height error due to an error in interferogram phase ($\Delta\phi$ resulting from the inaccurate estimate of deformation phase. We calculated the uncertainty of the estimated deformation during the summers of 1993 and 1995 to be less than 4 mm per 35 days, which corresponds to an interferometric phase value of 0.9 radians. This error will propagate into an error of less than 3 m in the preeruption DEM elevation with a low-frequency spatial characteristic.

The baseline vectors for all the interferograms were calculated using precision vectors (Massmann, 1995). The baseline vectors were further refined using the posteruption DEM from the SRTM data based on the approach described by Rosen et al. (1996) and using ground points with known elevation from SRTM. About 100 points were selected, all of them lying within the caldera but distant from the 1997 lava flows. We used a least squares approach to estimate the baseline components, and all ground points were weighted equally.

An unwrapped interferometric phase image together with the precision baseline vectors and imaging geometry were needed to derive the topographic heights. The following hierarchical approach, similar to the one proposed by Lanari et al. (1996), was used to facilitate the phase unwrapping procedure (Goldstein et al., 1988; Costantini, 1998). We started with the interferogram having the smallest baseline (i.e., the tandem pair acquired on October 25 and 26, 1995) (see Table 5.1). We first subtracted the topographic

phase from the interferogram using the SRTM DEM. The residual fringes were unwrapped (see Figure 5.4a), and the topographic phase was added back to this result. A DEM based on this tandem interferogram was then produced. Next, we unwrapped the August–September 1993 interferogram with $B_{\perp}$ = 403 m (see Table 5.1), because the coherence for this interferogram was better than the October–November 1993 pair (with $B_{\perp}$ = 395 m) (see Table 5.1). The simulated topographic phase based on the SRTM DEM was removed from the interferogram. The resulting residual interferogram

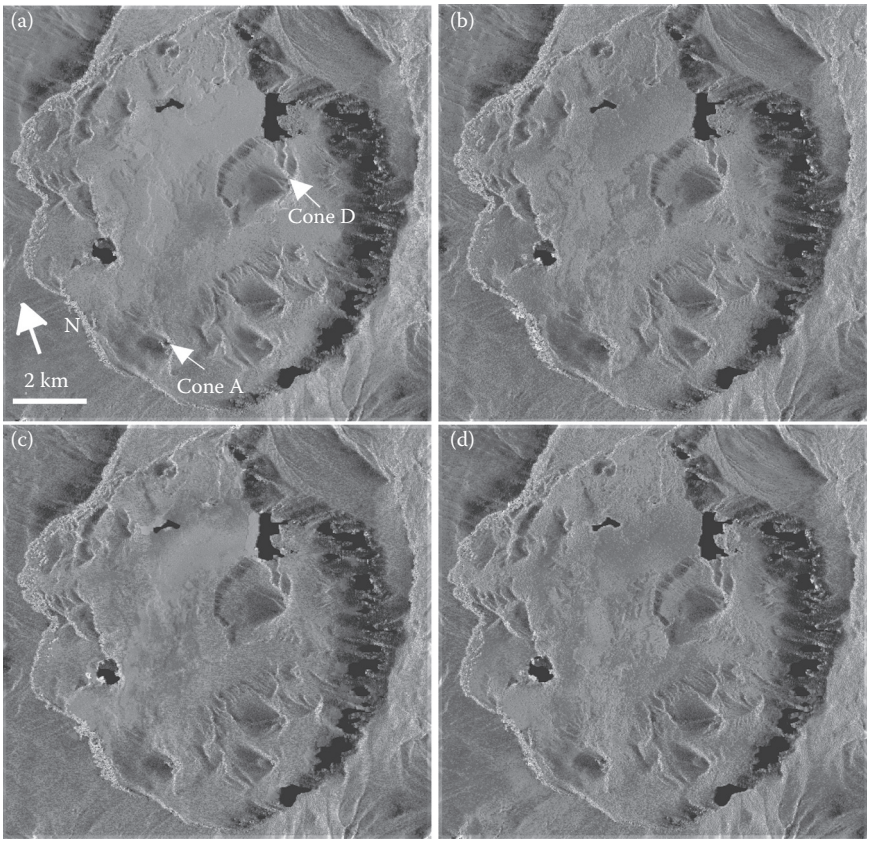

Figure 5.4 **(See color insert.)** Residual interferograms produced by subtracting the topographic phase from the original interferograms (see Table 5.1). (a) The tandem interferogram with $B_{\perp}$ = 83 m and the SRTM DEM was used to remove the topographic phase. (b) The interferogram with $B_{\perp}$ = 403 m and the SRTM DEM was used to remove the topographic phase. (c) The interferogram with $B_{\perp}$ = 395 m and the DEM produced from the interferogram with $B_{\perp}$ = 403 m was used to remove the topographic phase. (d) The interferogram with $B_{\perp}$ = 690 m and the DEM produced from the interferogram with $B_{\wedge}$ = 403 m was used to remove the topographic phase. A full cycle of colors represents a phase change of 360 degrees.

was unwrapped (see Figure 5.4b), and a DEM is generated. We did not use the DEM from the tandem interferogram to simulate the topographic phase because the SRTM is far more accurate than the DEM based on the tandem pair. The DEM from the tandem pair was produced from an interferogram with a smaller baseline. Consequently, the interferometric phase is not very sensitive to topographic relief and any possible atmospheric delay anomalies in the data will significantly bias the DEM accuracy. If an existing DEM is not available, however, the DEM produced from the interferogram with smaller baseline can be used to simulate the topographic phase in the interferogram with larger baseline. Finally, the DEM produced using the interferogram with $B_\perp = 403$ m (see Figure 5.4b) was then used to assist unwrapping the October–November 1993 pair (with $B_\perp = 395$ m) (see Figure 5.4c) and the interferogram with $B_\perp = 690$ m (see Figure 5.4d). Two more DEMs were produced. A simple weighted approach was used to combine the four DEMs:

$$h = \frac{\sum_{i=1}^{4} h_i c_i B_{\perp i}^2}{\sum_{i=1}^{4} c_i B_{\perp i}^2}, \tag{5.5}$$

where, h_i and c_i are height and coherence values from the four DEMs, and $B_{\perp i}$ is the perpendicular component of the baseline for each interferogram. The height value of each pixel in the final DEM results from the weighted average of the four DEMs, and height from the interferogram with larger baseline and higher coherence will be more heavily weighed. This procedure not only reduces the possible atmosphere-induced errors in each DEM but also improves accuracy of the final DEM. We used this procedure to generate a DEM depicting the topography of Okmok volcano before the 1997 eruption. A more sophisticated data-fusion technique, such as the wavelet method, can be used to combine DEMs from several interferograms with different spatial resolution, coherence, and vertical accuracy to generate the final DEM product (e.g., Ferretti et al., 1999; Lu et al., 2010b).

Figure 5.5a shows the thickness of the 1997 lava flows derived from the difference between the preeruption and the posteruption DEMs. We can see that the thickness of the lava is very heterogeneous. The thickest portion of the lava happens to be near the distal end (adjacent to Cone D) of the right arm of the Y-shaped flows, and reaches almost 50 m. The flow is thickest here because there was a substantial preexisting depression, which caused the flow to pond. In fact, this depression hides the extreme thickness in this area because the closest measurements of the flow margin's height do not exceed 20 m (Moxey et al., 2001). If the preeruption surface is not flat, measurements at the edges are not representative of total thickness.

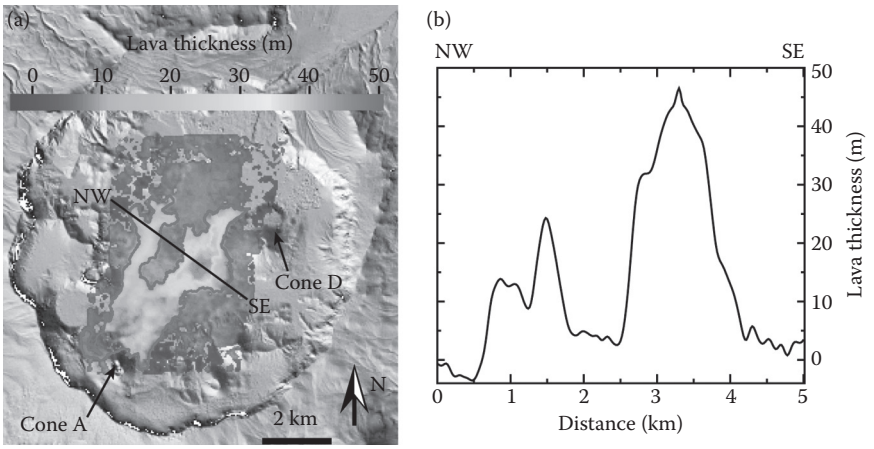

Figure 5.5 **(See color insert.)** Thickness of lava flows emplaced during the 1997 eruption at Okmok volcano, Alaska. (a) Flow thickness was derived from the height difference between the posteruption SRTM DEM and a preeruption DEM constructed from multi-temporal interferograms. (b) Lava thickness along profile northwest-southeast, reaching nearly 50 m in the thickest part of the flow. The red line represents the lava perimeter based on field data collected in August 2001. AQ1

Therefore, accurate DEMs are required to calculate more accurate values of lava thickness and eruption volume (e.g., Lu et al., 2003).

The standard deviation of our measurement can be estimated using the root-mean-square values of DEM difference over the areas outside of the lava flows. We estimate the mean and 1 σ uncertainty of the DEM difference to be 1.8 m and 2.6 m, respectively, after spatial averaging with a 100 m moving window filter. This means the DEM produced using the four ERS interferograms has a relative vertical accuracy of about 5 m at the 95% confidence limit.

5.3 DEM FROM MULTITEMPORAL INSAR PROCESSING

Multitemporal InSAR (MTInSAR)—that is, persistent scatterer InSAR (PSInSAR) or small baseline subset (SBAS) InSAR (Ferretti et al., 2001; Berardino et al., 2002; Rocca, 2007; Hooper, 2008)—is one of the most significant recent advances in InSAR processing. "Multi" in this context refers to a series of InSAR observations in time, thus affording the opportunity to recognize spurious effects. The objective is to fuse multiple-interferogram measurements of the same area to characterize the spatial and temporal behaviors of the deformation signal, the topography signal, and various

artifacts and noise sources (atmospheric delay anomalies, orbit errors), and then to remove the artifacts and anomalies to retrieve time-series deformation measurements as well as an accurate DEM height at the SAR pixel level.

Assuming we have more than about 20 repeat-pass SAR images, we can generate a stack of N coregistered multitemporal interferograms. Because our goal is to generate a new DEM or update an existing low-resolution or low-accuracy DEM, interferograms with short time separations and large baselines are preferred. This is critical to derive a high-accuracy DEM. If we generalize Equation 5.1 for a total of N interferograms, the phase value for the ith coherent pixel in the kth interferogram with a time separation of t^k, ϕ_i^k, can be expressed as the following (after the topographic contribution has been removed from an existing low-resolution DEM):

$$\phi_i^k = -\frac{4\pi}{\lambda}(v_i t^k + \mu_i^k) - \frac{4\pi}{\lambda}\frac{B_\perp^k h_i}{R^k \sin\theta^k} + \alpha_i^k + n_i^k . \tag{5.6}$$

The first term on the right side of Equation 5.6 represents the phase contribution related to ground surface deformation and consists of two components: one is due to the constant velocity (v_i), and the other is due to the nonlinear motion μ_i^k. The second term on the right side of Equation 5.6 represents the phase component due to DEM error (h_i) and is related to the perpendicular baseline ($B_\perp^k$), the distance from the master sensor to the scene center (R_k), and the SAR look angle (θ_k) at the scene center. α_i^k is the phase contribution due to atmospheric and baseline anomalies and the last term (n_i^k) is the decorrelation phase. Because multitemporal InSAR mainly focuses on coherent points, the noise term is expected to be small and Gaussian in the selected interferograms. It is worth noting that the aforementioned phase terms have different spatial-temporal characteristics, allowing us to separate the interested signals (i.e., DEM error and deformation velocity). By examining the unknown parameters, it becomes apparent that the DEM error and constant velocity do not change with time for each coherent pixel, whereas the remaining terms usually vary from interferogram to interferogram. Therefore, Equation 5.6 can be grouped into a time-invariant part and a time-variant part:

$$\phi_i^k = \left[\left(-\frac{4\pi}{\lambda}t^k\right)v_i + \left(-\frac{4\pi}{\lambda}\frac{B^k}{R^k \sin\theta^k}\right)h_i\right] + \left[-\frac{4\pi}{\lambda}\mu_i^k + \alpha_i^k + n_i^k\right]. \tag{5.7}$$

Let us look into the spatial characteristic of the time-variant part of Equation 5.7 in more detail, which is helpful to construct an optimal observation model for parameter estimation. Generally speaking, the phase component due to baseline inaccuracy in α_i^k effects interferograms in the form

of an almost-linear signal of long spatial wavelength. The other part of α_i^k, that is, the atmospheric phase, varies spatially with a typical scale of several kilometers. If we triangulate the coherent points in the study area and ensure that the length of the network edges (also called arcs) is less than a certain threshold (e.g., 1 km), the phase differences of α_i^k at the arcs will be limited to a low level (normally less than 0.1 rad[2]). Because the motions of neighboring pixels are normally correlated, the variance of nonlinear motion (μ_i^k) is also very small. Consequently, for a given arc, the sum of the time-variant parts in Equation 5.7 [now represented by $w_{x,y}^k$ in Equation 5.8 should be very small. An observation model of multitemporal InSAR for a given arc constructed by two neighboring coherent pixels (x, y) is thus defined as follows:

$$\Delta\phi_{x,y}^k = \left[\left(-\frac{4\pi}{\lambda}t^k\right)\Delta v_{x,y} + \left(-\frac{4\pi}{\lambda}\frac{B^k}{R^k \sin\theta^k}\right)\Delta h_{x,y}\right] + w_{x,y}^k. \tag{5.8}$$

Equation 5.8 indicates the relationship between the differential phase ($\Delta\varphi_{x,y}^k$) at the arc and the velocity difference ($\Delta v_{x,y}$) and height error difference ($\Delta h_{x,y}$), which is the basis for DEM refinement under the framework of MTInSAR. Because the observed differential phases are known only modulo 2π, the estimation of DEM error has to be performed either as a nonlinear inversion problem or as a linear problem, provided that the arcs with phase ambiguities can be reliably resolved or removed. Three approaches are introduced briefly here.

5.3.1 Two-dimensional solution search

As a nonlinear inversion problem, a search through the solution space must always be performed to estimate DEM errors as well as the deformation velocity from Equation 5.8. A temporal coherence index is commonly used for this inversion (Ferretti et al., 2001; Mora et al., 2003, Zhang et al., 2011b).

$$\gamma_{x,y} = \frac{1}{N}\left|\sum_{k=1}^{N} e^{-Jw_{x,y}^k}\right| = \frac{1}{N}\left|\sum_{k=1}^{N} e^{-J\left[\left(\Delta\phi_{x,y}^k + \left(\frac{4\pi}{\lambda}t^k\right)\Delta v_{x,y} + \left(\frac{4\pi}{\lambda}\frac{B^k}{R^k \sin\theta^k}\right)\Delta h_{x,y}\right)\right]}\right|, \tag{5.9}$$

where $J = \sqrt{-1}$. By setting proper variation ranges for velocity difference ($\Delta v_{x,y}$) and height error difference ($\Delta h_{x,y}$), one can search for the maximum coherence ($\gamma_{x,y}$) within the specified two-dimensional ranges using small sampling intervals. Then the optimum solutions of $\Delta v_{x,y}$ and $\Delta h_{x,y}$ can be found. After $\Delta v_{x,y}$ and $\Delta h_{x,y}$ between all neighboring pixels are determined,

the absolute values of DEM error and linear deformation rate at each coherent pixel can be derived through spatial integration with respect to a reference point at which the DEM error and linear deformation rate are known or assumed to be zero. The solution search can be successfully performed only under the condition of $\left|\omega^{k}_{i,x,y}\right| < \pi$, which can be met in most cases.

5.3.2 Linear inversion with phase ambiguity detector

Although temporal coherence maximization (see Equation 5.9) has the ability to resolve DEM errors from wrapped phase data, the method might result in several local maxima during the search of parameters (i.e., $\Delta v_{x,y}$ and $\Delta h_{x,y}$), which means a unique solution cannot be guaranteed. Because of possible phase ambiguities at some arcs, parameters cannot be estimated using a linear inversion (Zhang et al., 2011a). If ambiguities at troublesome arcs can be reliably removed, estimating parameters ($\Delta v_{x,y}$ and $\Delta h_{x,y}$) can be simplified significantly. Following is Equation 5.8 rewritten in a simplified vector form:

$$\Delta\Phi = \boldsymbol{A}\begin{bmatrix}\Delta h_{x,y}\\ \Delta v_{x,y}\end{bmatrix} + \boldsymbol{w}, \tag{5.10}$$

where $\Delta\Phi$ is the differential phase vector at a given arc constructed by two pixels x and y, $\boldsymbol{A}$ is the design matrix containing the coefficients of unknowns (i.e., $\Delta v_{x,y}$ and $\Delta h_{x,y}$), and $\mathbf{w}$ is a stochastic vector with an expectation of zero. For any arc regardless of phase ambiguities, the least squares solution of unknowns is as follows:

$$\begin{bmatrix}\Delta\hat{h}_{x,y}\\ \Delta\hat{v}\end{bmatrix} = (\boldsymbol{A}^{T}\boldsymbol{P}_{x,y}\ \boldsymbol{A})^{-1}\ \boldsymbol{A}^{T}\boldsymbol{P}_{x,y}\ \Delta\Phi$$
$$\boldsymbol{r} = \Delta\Phi - \boldsymbol{A}\ (\boldsymbol{A}^{T}\boldsymbol{P}_{x,y}\ \boldsymbol{A})^{-1}\ \boldsymbol{A}^{T}\boldsymbol{P}_{x,y}\ \Delta\Phi, \tag{5.11}$$

where $\boldsymbol{r}$ is the least squares residual vector and $P_{x,y}$ is the weight matrix which can be obtained by taking the inverse of a prior variance matrix of the double-difference phases (Zhang et al., 2011a). It has been observed that the least squares residuals for an arc with and without phase ambiguities are quite different (see Figure 5.6), indicating that phase ambiguities can bias the parameter estimation significantly. An ambiguity detector therefore can be designed according to the least squares residuals. The details can be found in Zhang et al. (2011a). After removing the arcs with phase ambiguities, parameters at the remaining arcs are integrated to obtain the parameter estimates at all coherent points with respect to a reference point.

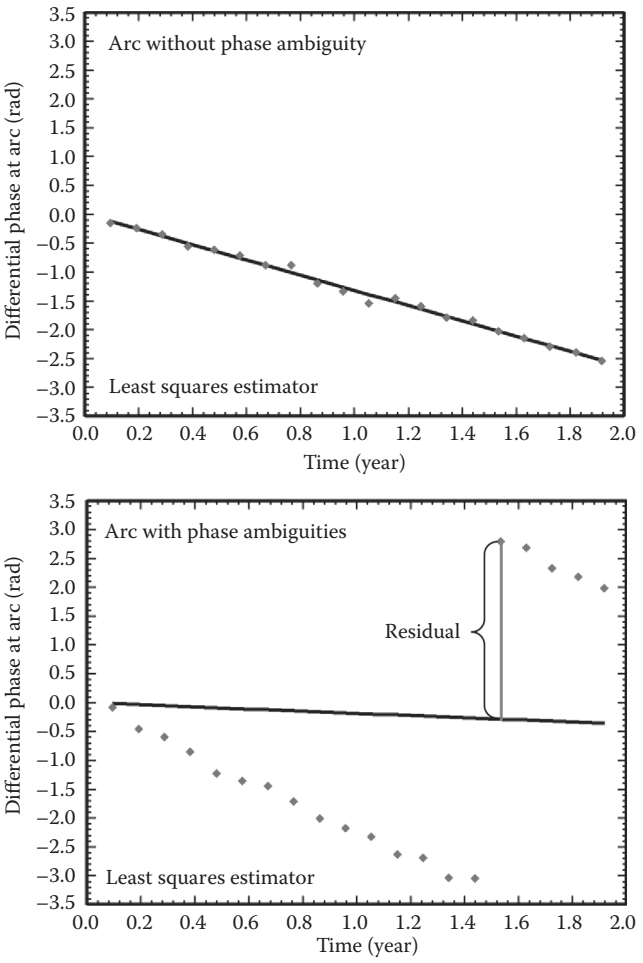

Figure 5.6 Least squares residuals at an arc with and without phase ambiguity. For illustrative purpose, only one parameter is estimated.

5.3.3 Linear inversion with phase unwrapping

Besides the removal of arcs with phase ambiguities, there is another way to linearly estimate DEM errors as well as deformation rates. Provided that two-dimensional phase unwrapping can be reliably performed on each interferogram, estimating parameters turns out to be a simple least squares problem where no ambiguity detector is needed:

$$\begin{bmatrix} \Delta\hat{h}_{x,y} \\ \Delta\hat{v} \end{bmatrix} = (\boldsymbol{A}^{T}\boldsymbol{P}_{x,y}\ \boldsymbol{A})^{-1}\ \boldsymbol{A}^{T}\boldsymbol{P}_{x,y}\ \Delta\Phi_{\text{unwraped}}. \tag{5.12}$$

Parameters at pixels can be achieved by integration as done in the aforementioned approaches. Although the solution form of Equation 5.12 is similar to the one in small baseline subset SBAS InSAR method (Berardino et al., 2002), there is an essential difference: SBAS takes phases at pixels as observations whereas this model takes the differential phases at arcs as observations. The latter can better suppress the effects of atmospheric anomalies (Zhang et al., 2011a).

Figure 5.7 shows the DEM error map of Okmok volcano derived from MTInSAR processing. This DEM error map is based on a DEM constructed from a two-antenna airborne InSAR system (Lu et al., 2003). Because the airborne system typically images an area of about 10 km wide, multiple DEMs from several flight passes were used to generate the DEM mosaic. However, the original DEM patches have systematic errors of ±50m (Lu et al., 2003). These errors result in some artifacts in the DEM mosaic over the western flank of the volcano. The MTInSAR technique can correct the DEM error (see Figure 5.7) and produce a better DEM for Okmok volcano.

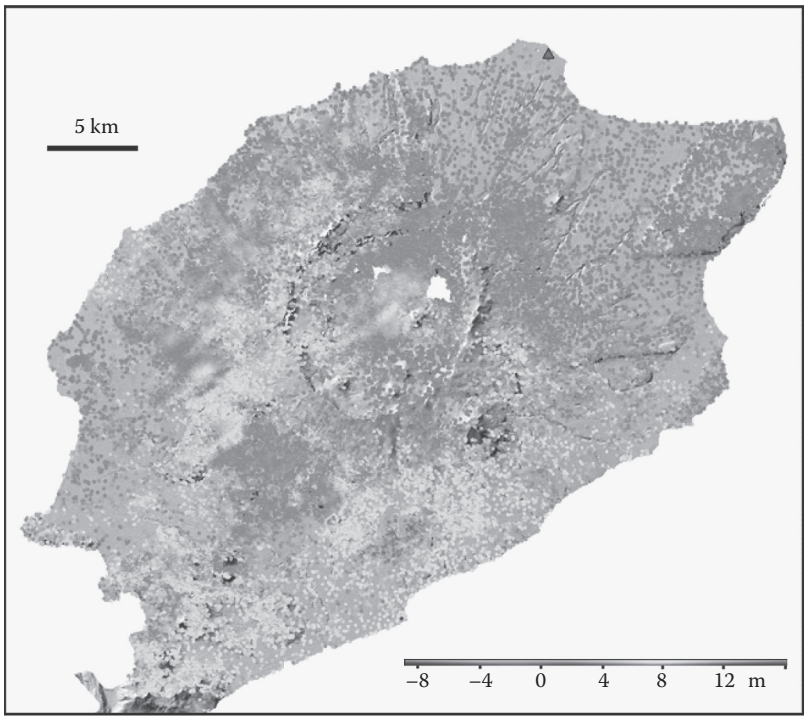

Figure 5.7 DEM height update from MTInSAR processing technique for Okmok volcano, Alaska. The height difference is with respect to an airborne DEM mosaic.

5.4 DEM FROM ENVISAT/ERS-2 CROSS-PLATFORM INSAR

As discussed and illustrated in previous sections, a rule of thumb on generating DEMs from repeat-pass InSAR imagery is to select interferograms with the largest available baselines within the limit of correlation. That is because the DEM accuracy is inversely proportional to the baseline length (Equation 5.2). We have demonstrated that the vertical resolution of DEMs derived from repeat-pass InSAR imagery can reach to a few meters if multitemporal interferograms are available. Therefore, it is generally impossible to generate a DEM with submeter accuracy, which requires the InSAR baseline to be larger than the critical baseline.

Generally speaking, a SAR system images the ground surface at a specific radar carrier frequency and incidence angle. A change in radar incidence angle (which translates to a change in baseline) or radar carrier frequency can result in a change in the radar reflectivity spectrum in range direction. The change in radar reflectivity spectrum (Δf) can be defined as follows (Gatelli et al., 1994):

$$\Delta f = -\frac{cB_{\perp}}{\lambda R \tan(\theta - \alpha)}, \tag{5.13}$$

where c is speed of light and α is the terrain slope angle.

If two SAR images used to create an InSAR image are from SAR systems of the same carrier frequency, the change in radar reflectivity spectrum in range direction needs to be small so that the reflectivity spectra of the two signals overlap, which translates to the requirement of $B_{\perp}$ < the critical baseline. There is, however, a condition under which the effect of the baseline can be exactly compensated by a difference in radar frequency between two SAR acquisitions (Gatelli et al., 1994; Guarnieri and Prati, 2000; Colesanti et al., 2003). From Equation 5.13, for a given frequency difference, the perpendicular baseline component ($B_{\perp}$) required to compensate for the frequency difference can be defined as follows:

$$B_{\perp} \approx -\frac{(f_2 - f_1)\, R \tan(\theta - \alpha)}{f_1}, \tag{5.14}$$

where f_1 and f_2 are radar carrier frequencies of two SAR acquisitions.

Acquisitions from C-band Envisat and ERS-2 SARs from ESA were on the same orbital plane with a 35-day repeat and a 28-minute time lag. The radar frequency of Envisat, however, is slightly different from that of ERS-2 by 31 megahertz (MHz). Because of this difference, Envisat SAR images generally cannot be combined with ERS-2 data for repeat-pass cross-platform InSAR processing. Fortunately, the 31 MHz frequency difference between ERS-2 and Envisat SAR images can be compensated by a

perpendicular baseline of approximately 2 km over a flat surface (Equation 5.14). Consequently, Envisat and ERS-2 can be combined to preserve InSAR coherence in spite of a large baseline of about 2 km. For an interferogram of $B_{\perp} = 2$ km, one interferometric fringe corresponds to a topographic relief of ~4.8 m (Equation 5.3). Therefore, an Envisat/ERS-2 cross-platform InSAR image is capable of generating a submeter-accuracy DEM. Because the two SAR images are acquired about 28 minutes apart, temporal decorrelation as well as atmospheric artifacts are significantly reduced (Wegmuller et al., 2009).

We demonstrate the DEM generation using a pair of Envisat/ERS-2 images acquired on January 25, 2008, over northern Alaska (see Table 5.2). The exiting DEM from the USGS National Elevation Dataset (NED), with a posting of 2-arc-second and vertical accuracy of several meters, are also used in InSAR processing. We generated Envisat and ERS-2 SLC images using the same Doppler centroid and Doppler bandwidth calculated by the azimuth common band filtering to minimize the misregistration, and then we oversampled SLC images twice to reduce the phase unwrapping error. After DEM-assisted coregistration of Envisat and ERS-2 SLC images (Lee et al., 2010), the Envisat/ERS-2 cross-platform interferogram is created. The interferogram is unwrapped and converted into a topographic height map (see Figure 5.8a).

To assess the vertical accuracy of the Envisat/ERS-2 cross-platform InSAR-derived DEM, we compared it with an airborne DEM produced in July 2002, which has a spatial resolution of 5 m and vertical height specification of 10 cm. We selected an area in Figure 5.8a for accuracy assessment. The average height of the area is about 80 m. Figures 5.8b and 5.8c show the InSAR-derived DEM and the airborne DEM, and Figure 5.8d represents the height difference between the two DEMs along profile *A*-*A*'. The mean and standard deviation of the difference over the study area are 1 cm and 39 cm, respectively. Figure 5.8e shows the histogram of the height difference. The histogram generally follows a Gaussian distribution with no bias. From this comparison, we conclude the vertical accuracy of the DEM from Envisat/ERS-2 cross-platform InSAR is less than 40 cm.

This method of cross-platform InSAR utilizing the baseline difference to compensate the difference in SAR central frequency requires two similarly configured SAR systems on two separate platforms to generate interferograms with a baseline large enough to be sensitive to terrain height to

Table 5.2 Characteristics of ERS-2 and envisat pair for cross-platform InSAR

Parameters	*ERS-2*	*Envisat*
Central frequency (MHz) (GHz)	5.3	5.331
Acquisition date	January 25, 2008	
Time interval (min.)	28 minutes (Envisat – ERS2)	
$B_{\perp}$ (m)	2,400	

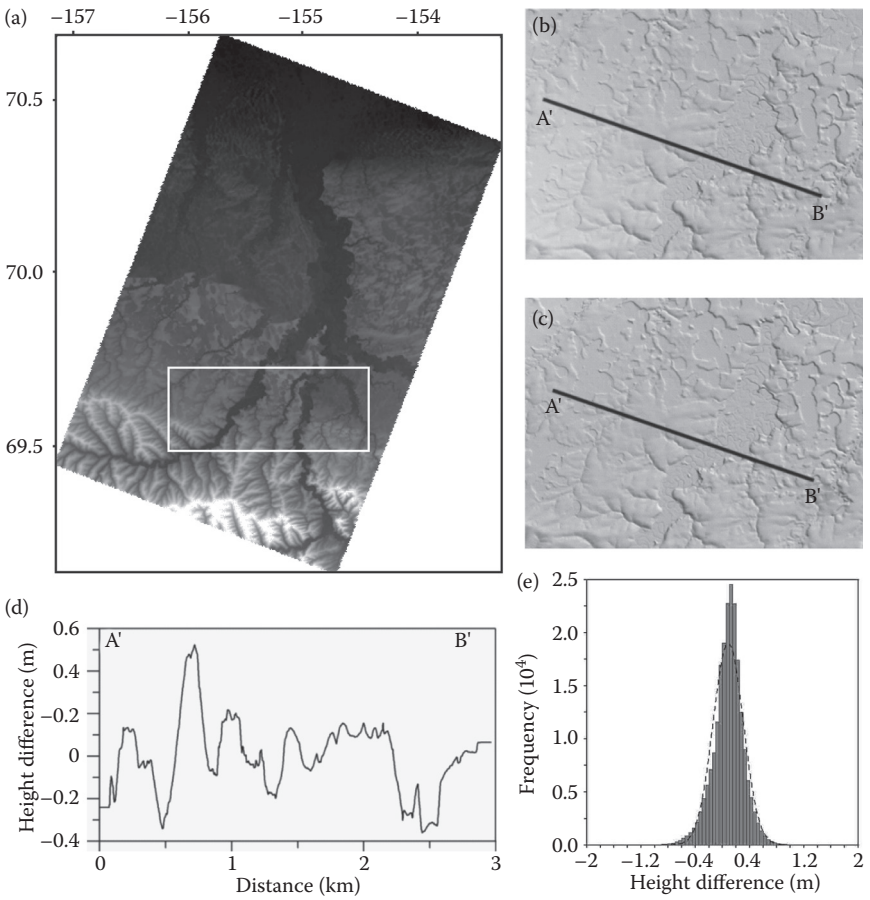

Figure 5.8 (a) Envisat/ERS-2 cross-platform InSAR-derived DEM over northern Alaska. Comparison of the InSAR-derived DEM (b) and a high-resolution airborne DEM (c) over an area outlined by the while rectangle in (a). (d) Height difference between the InSAR-derived DEM and the airborne DEM along profile of A'-B'. (e) Histogram of height differences between the Envisat/ERS-2 InSAR-derived DEM and the airborne DEM.

submeter accuracy. Such accurate DEM generation is the ultimate objective for the current DLR TanDEM-X mission.

5.5 DEM FROM TanDEM-X

The TerraSAR-X tandem mission for DEM measurements, TanDEM-X, was launched by DLR in 2010 (http://www.dlr.de/hr/en/desktopdefault.aspx/tabid-2317). TanDEM-X is a new high-resolution constellation InSAR mission that relies on an innovative flight formation of two tandem TerraSAR-X

satellites to produce InSAR-derived DEMs on a global scale with accuracy better than SRTM (Krieger et al., 2007). In addition, TanDEM-X can enable precise mapping of ocean currents by fusing two SAR images steered in the along-track direction. The resulting product will be invaluable for monitoring extreme waves and ocean hazards. Furthermore, TanDEM-X will provide data to assess the utility of new methods, including bistatic multiangle SAR imaging, digital beam formation, and polarimetric InSAR, for monitoring landscape changes.

The two X-band SARs on two separate TerraSAR-X satellites record data synchronously and create a baseline ranging from ~200 m to ~500 m. The precise baseline determination and simultaneous data acquisitions can generate InSAR images that are immune to baseline errors, atmospheric contaminations, and temporal decorrelation that plague the accuracy of DEMs derived from repeat-pass InSAR. Therefore, the TanDEM-X satellite constellation allows the generation of global DEMs of an unprecedented accuracy, coverage, and quality. TanDEM-X DEMs have a specified relative vertical accuracy of 2 m and an absolute vertical accuracy of 10 m at a horizontal resolution of 12 m (Krieger et al., 2007).

5.6 CONCLUSION

The ideal SAR configuration for accurate DEM production is a single-pass (simultaneous) two-antenna system. Repeat-pass single-antenna satellite InSAR can be used to produce useful DEMs, particularly in areas where the photogrammetric approach to DEM generation is hindered by persistent clouds or other factors. There are many sources of errors in DEM construction from repeat-pass SAR images, including inaccurate determination of the InSAR baseline, atmospheric delay anomalies, and possible surface deformation resulting from tectonic, volcanic, or other sources during the time interval spanned by the images. To generate a high-quality DEM, these errors must be identified and corrected using a multi-interferogram approach. A data fusion technique such as PSInSAR or SBAS InSAR can be applied to a stack of repeat-pass InSAR images to generate a DEM accurate to meters. Ultimately, special InSAR image formation from constellation satellites, such as TanDEM-X, will continue advancing the spatial resolution and vertical accuracy of the global DEM.

ACKNOWLEDGMENTS

ERS-1, ERS-2, and Envisat SAR images are copyright © ESA, and provided by ESA and the Alaska Satellite Facility. This work was supported by the USGS Volcano Hazards Program and the NASA's Earth Surface and

Interiors Program (2005–0021). We thank Dave Ramsey and Russ Rykhus for careful edits and constructive review.

REFERENCES

Berardino, P., G. Fornaro, R. Lanari, and E. Sansosti. 2002. A new algorithm for surface deformation monitoring based on small baseline differential SAR interferograms. *IEEE Transactions on Geoscience and Remote Sensing* 40: 2375–2383.

Colesanti, C., F. De Zan, A. Ferretti, C. Prati, and F. Rocca. 2003. Generation of DEM with sub-metric vertical accuracy from 30′ ERS–ENVISAT pairs. In *Proceedings from Fringe 2003 Workshop*. Frascati, Italy: ESA-ESRIN.

Costantini, M. 1998. A novel phase unwrapping method based on network programming. *IEEE Transactions on Geoscience and Remote Sensing* 36: 813–821.

Emardson, T. R., M. Simons, and F. H. Webb. 2003. Neutral atmospheric delay in interferometric synthetic aperture radar applications: statistical description and mitigation. *Journal of Geophysical Research* 108: 2231. doi:10.1029/2002JB001781.

Farr, T. G., et al. 2007. The Shuttle Radar Topography Mission. *Reviews of Geophysics* 45: RG2004. doi:10.1029/2005RG000183. AQ2

Ferretti, A., C. Prati, and F. Rocca. 1999. Multibaselime InSAR DEM Reconstruction: the wavelet approach. *IEEE Transactions on Geoscience and Remote* Sensing 37: 705–715.

Ferretti, A., C. Prati, and F. Rocca. 2001. Permanent scatterers in SAR interferometry. *IEEE Transactions on Geoscience and Remote Sensing* 39:8–20.

Foster, J., et al. 2006. Mitigating atmospheric noise for InSAR using a high-resolution weather model. *Geophysical Research Letters* 33: L16304. doi:10.1029/2006GL026781. AQ3

Gabriel, A., R. Goldstein, and H. Zebker. 1989. Mapping small elevation changes over large areas: differential radar interferometry. *Journal of Geophysical Research* 94: 9183–9191.

Gatelli, F., et al. 1994. The wavenumber shift in SAR interferometry. *IEEE Transactions on Geoscience and Remote Sensing* 31: 855–865. AQ4

Goldstein, R. 1997. Atmospheric limitations to repeat-track radar interferometry. *Geophysical Research Letters* 22: 2517–2520.

Goldstein, R., H. Zebker, and C. Werner. 1988. Satellite radar interferometry: two-dimensional phase unwrapping. *Radio Science* 23: 713–720.

Gong, W., F. Meyer, P. Webley, and Z. Lu. 2011. Methods of InSAR atmosphere correction for volcano activity monitoring. In *Proceedings of 2011 IGARSS* 4. Vancouver, Canada. AQ5

Gray, A. L., K. E. Mattar, and G. Sofko. 2000. Influence of ionospheric electron density fluctuations on satellite radar interferometry. *Geophysical Research Letters* 27: 1451–1454.

Guarnieri, A. M., and C. Prati. 2000. ERS-ENVISAT combination for interferometry and super-resolution. In *Proceedings of ERS-ENVISAT Symposium*. AQ6

Hensley, S., R. Munjy, and P. Rosen. 2001. Interferometric synthetic aperture radar (IFSAR). In *Digital Elevation Model Technologies and Applications: The*

AQ7 *DEM Users Manual*, edited by D. F. Maune, 143–206. American Society for Photogrammetry and Remote Sensing.

Hooper, A. 2008. A multi-temporal InSAR method incorporating both persistent scatterer and small baseline approaches. *Geophysical Research Letters* 35: L16302. doi:10.1029/2008GL034654.

AQ8 Krieger, G., et al. 2007. TanDEM-X: a satellite formation for high-resolution SAR interferometry. *IEEE Transactions on Geoscience and Remote Sensing* 45: 3317–3341.

AQ9 Lanari, R., et al. 1996. Generation of digital elevation models by using SIR-C/X-SAR multifrequency two-pass interferometry: the Etna case study. *IEEE Transactions on Geoscience and Remote Sensing* 34: 1097–1114.

Lee, W. J., H. S. Jung, and Z. Lu. 2010. A study of high-precision DEM generation using ERS-Envisat SAR cross-interfeometry. *Journal of Korean Society of Surveying, Geodesy, Photogrammetry and Cartography* 28: 431–439.

Li, Z., J. P. Muller, and P. Cross. 2003. Comparison of precipitable water vapor derived from radiosonde, GPS, and Moderate-Resolution Imaging Spectroradiometer measurements. *Journal of Geophysical Research* 108: 4651. doi:10.1029/2003JD003372.

Lu, Z. 2007. InSAR imaging of volcanic deformation over cloud-prone areas: Aleutian Islands. *Photogrammetric Engineering and Remote Sensing* 73: 245–257.

Lu, Z., and W. Danskin. 2001. InSAR analysis of natural recharge to define structure of a ground-water basin, San Bernardino, California. *Geophysical Research Letters* 28: 2661–2664.

Lu, Z., D. Dzurisin, J. Biggs, C. Wicks, and S. McNutt. 2010a. Ground surface deformation patterns, magma supply, and magma storage at Okmok volcano, Alaska, from InSAR analysis: 1. intereruption deformation, 1997–2008. *Journal of Geophysical Research-Solid Earth* 115(B00B02): doi:10.1029/2009JB006969.

Lu, Z., D. Dzurisin, H. S. Jung, J. X. Zhang, and Y. H. Zhang. 2010b. Radar image and data fusion for natural hazards characterization. *International Journal of Image and Data Fusion* 1: 217–242.

Lu, Z., E. Fielding, M. Patrick, and C. Trautwein. 2003. Estimating lava volume by precision combination of multiple baseline spaceborne and airborne interferometric synthetic aperture radar: the 1997 eruption of Okmok volcano, Alaska. *IEEE Transactions on Geoscience and Remote Sensing* 41: 1428–1436.

Lu, Z., and J. Freymueller. 1998. Synthetic aperture radar interferometry coherence analysis over Katmai volcano group, Alaska. *Journal of Geophysical Research* 103: 29887–29894.

Lu, Z., O. Kwoun, and R. Rykhus. 2007. Interferometric synthetic aperture radar (InSAR): its past, present and future. *Photogrammetric Engineering and Remote Sensing* 73: 217–221.

Lu, Z., D. Mann, and J. Freymueller. 1998. Satellite radar interferometry measures deformation at Okmok volcano. *EOS Transactions* 79: 461–468.

Lu, Z., D. Mann, J. Freymueller, and D. Meyer. 2000. Synthetic aperture radar interferometry of Okmok volcano, Alaska: radar observations. *Journal of Geophysical Research* 105: 10791–10806.

Lu, Z., T. Masterlark, and D. Dzurisin. 2005. Interferometric Synthetic Aperture Radar (InSAR) study of Okmok volcano, Alaska, 1992–2003: magma supply dynamics and post-emplacement lava flow deformation. *Journal of Geophysical Research* 110: B02403. doi:10.1029/2004JB003148.

Massmann, F. H. 1995. Information for ERS PRL/PRC Users. *GeoForschungsZentrum Potsdam Technical Note*.

Massonnet, D., and K. Feigl. 1998. Radar interferometry and its application to changes in the Earth's surface. *Reviews of Geophysics* 36: 441–500.

Maune, D. 2001. *Digital Elevation Model Technologies and Applications: The DEM Users Manual*. American Society for Photogrammetry and Remote Sensing. AQ10

Miller, T. P., et al. 1998. Catalog of the historically active volcanoes of Alaska. *USGS Open-File Report*, 98–582. AQ11

Mogi, K. 1958. Relations between the eruptions of various volcanoes and the deformations of the ground surface around them. *Bulletin of the Earthquake Research Institute of the University of Tokyo* 36: 99–134.

Mora, O., J. J. Mallorqui, and A. Broquetas. 2003. Linear and nonlinear terrain deformation maps from a reduced set of interferometric SAR images. *IEEE Transactions on Geoscience and Remote Sensing* 41: 2243–2253.

Moxey, L. 2001. The 1997 eruption of Okmok volcano, Alaska, a synthesis of remotely sensed data. *EOS Transactions* 82: 47. AQ12

Rocca, F. 2007. Modeling interferogram stacks. *IEEE Transactions on Geoscience and Remote Sensing* 45: 3289–3299.

Rosen, P., S. Hensley, H. Zebker, F. H. Webb, and E. J. Fielding. 1996. Surface deformation and coherence measurements of Kilauea volcano, Hawaii, from SIR-C radar interferometry. *Journal of Geophysical Research* 101: 23109–23125.

Rosen, P., et al. 2000. Synthetic aperture radar interferometry. *Proceedings of IEEE* 88: 333–380. AQ13

Ruffino, G., A. Moccia, and S. Esposito. 1998. DEM generation by means of ERS tandem data. *IEEE Transactions on Geoscience and Remote Sensing* 36: 1905–1912

Rykhus, R., and Z. Lu. 2008. InSAR detects possible thaw settlement in the Alaskan Arctic Coastal Plain. *Canadian Journal of Remote Sensing* 34: 100–112.

Sansosti, E., et al. 1999. Digital elevation model generation using ascending and descending ERS-1/ERS-2 tandem data. *International Journal of Remote Sensing* 20: 1527–1547. AQ14

Small, D., C. Werner, and D. Muesch. 1995. Geocoding and validation of ERS-1 InSAR-derived digital elevation models. *ERSSeL Advanced Remote Sensing* 4: 26–39.

Wegmuller, U., S. Maurizio, C. Werner, and T. Strozzi. 2009. DEM generation using ERS-Envisat interferometry. *Journal of Applied Geophysics* 69: 51–58.

Zebker, H. A., et al. 1992. The TOPSAR interferometric radar topographic mapping instrument. *IEEE Transactions on Geoscience and Remote Sensing* 30: 933–940. AQ15

Zebker, H. A., C. L. Werner, P. A. Rosen, and S. Hensley. 1995. Accuracy of topographic maps derived from ERS-1 interferometric radar. *IEEE Transactions on Geoscience and Remote Sensing* 32: 823–836.

Zhang, L., X. L. Ding, and Z. Lu. 2011a. Modeling PSInSAR time series without phase unwrapping. *IEEE Transactions on Geoscience and Remote Sensing* 49: 547–556.

Zhang, Y. H., J. X. Zhang, H. A. Wu, Z. Lu, and G. T. Sun. 2011b. Monitoring of urban subsidence with SAR interferometric point target analysis: a case study in Suzhou, China. *International Journal of Applied Earth Observation and Geoinformation* 13: 812–818.